Available online at www.sciencedirect.com
ScienceDirect
International Journal of Heat and Mass Transfer 49 (2006) 4867–4876
International Journal of HEAT and MASS TRANSFER
www.elsevier.com/locate/ijhmt

Two-temperature chemically-non-equilibrium modeling of argon induction plasmas with diatomic gas

Takayuki Watanabe [a,*], Masaya Shigeta [a], Nobuhiko Atsuchi [b]

[a] Department of Environmental Chemistry and Engineering, Tokyo Institute of Technology, 4259-G1-22 Nagatsuta Midori-ku Yokohama 226-8502, Japan
[b] Department of Nuclear Engineering, Tokyo Institute of Technology, 2-12-1 Ookayama Meguro-ku, Tokyo 152-8550, Japan

Received 10 February 2006
Available online 1 September 2006

Abstract

A non-equilibrium modeling of argon–oxygen and argon–hydrogen induction thermal plasmas was performed without thermal and chemical equilibrium assumptions. Reaction rates of dissociation and recombination of diatomic gas and ionization were taken into account with two-temperature modeling. A substantial deviation from LTE exists near the torch wall in argon–oxygen induction plasmas under atmospheric pressure, while small deviation in argon–hydrogen plasmas results from the large collision frequency between electrons and hydrogen atoms.

Keywords: Induction thermal plasma; Numerical modeling; Argon–Oxygen; Argon–Hydrogen; Non-equilibrium; Two-temperature

1. Introduction

The induction thermal plasma approach has been applied for production of high-quality and high-performance materials, such as synthesis of nanoparticles, deposition of thin films, and plasma spraying. Another attractive application is treatment of harmful waste materials and recovery of useful material from wastes. These applications are based on the unique advantages of induction thermal plasmas; high-enthalpy to enhance reaction kinetics, high-chemical reactivity, oxidation and reduction atmospheres in accordance with required chemical reactions, and rapid quenching ($\sim 10^6$ Ks^{-1}). These advantages provide chemically reactive flow rather than simply high-temperature flow for thermal plasmas.

Sophisticated modeling considering chemical reactions has been required for industrial applications, because thermal plasmas with adding reactive gas are desirable to enhance the chemical reactivity of the plasma in material processing and environmental processing. However, thermal plasmas have been mainly treated as local thermodynamic equilibrium (LTE) conditions. The purpose of this work is to develop two-temperature chemically-non-equilibrium (2T-CNE) modeling of induction thermal plasmas.

In the previous works using the non-equilibrium modeling for chemical reactions, some modeling works were reported for induction thermal plasmas considering dissociation and recombination with finite-rates of diatomic gas in argon plasmas with one-temperature model [1–9]. In addition, modeling of induction thermal plasmas including two-temperature conditions has been carried out: two-temperature model of argon plasmas [10], two-temperature with dissociation and recombination as well as the ionization of argon–nitrogen plasmas [11]. In these works, estimation of thermodynamic and transport properties was oversimplified. The oversimplified estimation, such as use of equilibrium properties or the first-order approximation of Chapman–Enskog method, would cause errors in the numerical results, therefore more sophisticated models are required. In order to improve the accuracy of thermodynamic and transport properties, the higher-order approximation of

* Corresponding author. Tel./fax: +81 45 924 5414.
E-mail address: watanabe@chemenv.titech.ac.jp (T. Watanabe).

0017-9310/$ - see front matter © 2006 Elsevier Ltd. All rights reserved.
doi:10.1016/j.ijheatmasstransfer.2006.05.039

Nomenclature

$\mathbf{B}$	magnetic flux density [T]
D_i^{m}	effective diffusion coefficient [$m^2\ s^{-1}$]
E_{eh}	energy exchange between electron and heavy particle [$W\ m^{-3}$]
$\mathbf{E}$	electric field [$V\ m^{-1}$]
h	enthalpy [$J\ kg^{-1}$]
$\mathbf{J}$	current density [$A\ m^{-2}$]
k	Boltzmann constant [$J\ K^{-1}$]
k_{f}	reaction rate constant for forward reaction [$cm^3\ mol^{-1}\ s^{-1}$]
K	equilibrium constant [m^{-3}]
m_i	mass of species i [kg]
n_i	number density of species i [m^{-3}]
p	pressure [Pa]
q_{r}	radiative intensity [$W\ m^{-3}$]
ΔQ_l	reaction heat due to reaction l [$W\ m^{-3}$]
r	radial position [m]
r_{w}	inner radius of torch wall [m]
$R_{\mathrm{r}i}$	production rate of species i [$kg\ m^{-3}\ s^{-1}$]
T	temperature [K]
$\mathbf{u}$	velocity [$m\ s^{-1}$]
Y_i	mass fraction of species i [–]
Γ	mass flux of electrons due to diffusion [$kg\ m^{-2}\ s^{-1}$]
δ^{D}	degree of chemical non-equilibrium due to dissociation [–]
δ^{I}	degree of chemical non-equilibrium due to ionization [–]
$\lambda_{\mathrm{tr}}^{\mathrm{h}}$	translational thermal conductivity due to heavy particle [$W\ m^{-1}\ K^{-1}$]
$\lambda_{\mathrm{tr}}^{\mathrm{e}}$	translational thermal conductivity due to electron [$W\ m^{-1}\ K^{-1}$]
ν_{ei}	collision frequency between electrons and heavy particles [s^{-1}]
ζ	Damkohler number [–]
ρ	density [$kg\ m^{-3}$]
τ_{d}	characteristic diffusion time [s]
τ_{r}	characteristic reaction time [s]
$\boldsymbol{\tau}$	stress tensor [Pa]
$\overline{\Omega}_{ij}^{(i,j)}$	collision integral between species i and j [m^2]

Subscripts

Ar	argon
Ar^+	argon ion
e	electron
h	heavy particle
H_2	hydrogen molecule
H^+	hydrogen atom ion
O_2	oxygen molecule
O^+	oxygen atom ion
i,j	chemical species

Chapman–Enskog method was used for estimation of the transport properties of oxygen plasmas [8,9]. They presented that the thermal conductivity and the electrical conductivity obtained from the higher-order approximation differed from those of the first-order approximation over 10,000 K.

In this study, a non-equilibrium modeling of argon–oxygen and argon–hydrogen induction thermal plasmas was developed without thermal and chemical equilibrium assumptions. The formulation including the two-temperature state and the finite-rates of dissociation and ionization is presented using the higher-order approximation of Chapman–Enskog method for estimation of the transport properties. The non-equilibrium effect on argon–oxygen plasma and argon–hydrogen plasma characteristics will be discussed with comparison between the Two-temperature chemically-non-equilibrium (2T-CNE) and the One-temperature chemically-equilibrium (1T-CE, or LTE) models. Characteristics of thermal and chemical non-equilibrium will also be discussed.

2. Numerical formulation

2.1. Thermodynamic and transport properties

The transport properties of argon–oxygen and argon–hydrogen plasmas were obtained from Chapman–Enskog method. Up to now, modeling of induction thermal plasmas has been mainly performed with the first-order approximation of Chapman–Enskog method since the higher-order of Sonine polynomial expansion requires many kinds of collision integrals resulting in the complex formula. The first-order approximation may cause errors especially for electrical conductivity and thermal conductivity of the electron translational contribution at high-temperature. Therefore, the higher-order approximation is used according to the required accuracy. In the CNE model, the transport and thermodynamic properties are strongly related to the temperature and the composition of the plasma. Therefore, the transport and thermodynamic properties should be estimated considering the diffusion of the species in the plasma at each calculation step until the convergence. Compared with the complex formulae in the 2T-CNE model, the transport and thermodynamic properties are simple functions of only temperature in the 1T-CE model. Detailed estimation can be found in Ref. [9].

The total thermal conductivity consists of the reactive conductivity and the "chemically frozen" conductivity including the translational and the internal one. The reactive and internal conductivities were estimated with the first-order approximation of Chapman–Enskog method [12,13]. The translational thermal conductivity contains

the contribution of heavy particles estimated with the second-order approximation of Chapman–Enskog method [14] and electrons with the third-order approximation as the suggestion by Devote [15]. Concentration dependence of the thermal conductivity with oxygen or hydrogen injection was shown in Fig. 1. The thermal conductivity has high-values where dissociation and ionization occur. The thermal conductivity increases with hydrogen addition because of the small mass of hydrogen.

The viscosity was estimated with the first-order approximation of Chapman–Enskog method [12]. Concentration dependence of the viscosity with oxygen addition and hydrogen addition was shown in Fig. 2. The viscosity has the maximum at 10,000 K where the ionization begins to play important roles. In mixture of argon and hydrogen, the viscosity decreases with hydrogen addition due to the small mass of hydrogen.

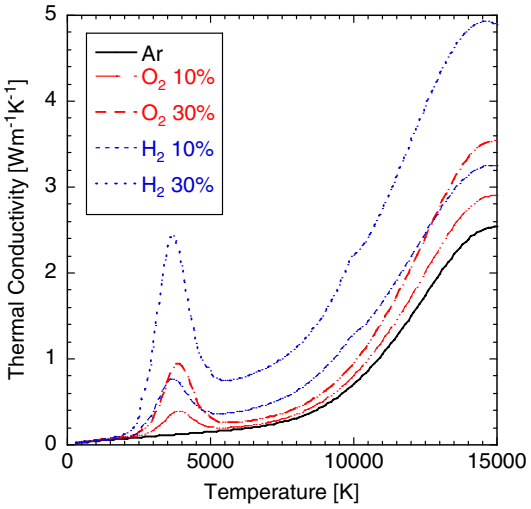

Fig. 1. Thermal conductivity of argon–oxygen and argon–hydrogen mixture.

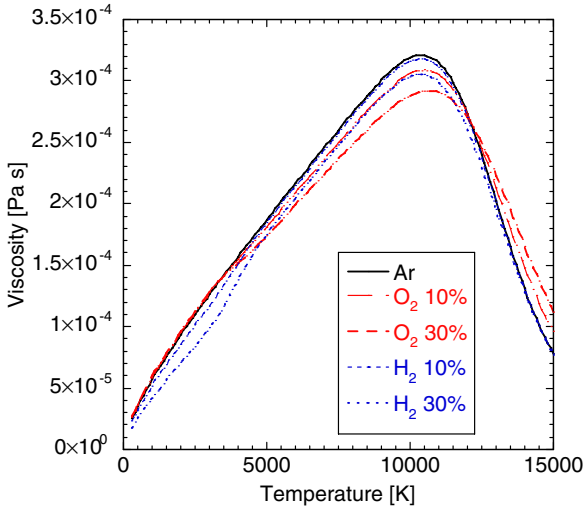

Fig. 2. Viscosity of argon–oxygen and argon–hydrogen mixture.

The thermodynamic properties, the enthalpy and the specific heat at constant pressure, were obtained from the equilibrium properties. This is oversimplification, however the accurate estimation of the non-equilibrium thermodynamic properties is very complex with satisfying the self-consistent conditions.

2.2. Kinetic rate constants

Tables 1 and 2 summarize the reactions in the argon–oxygen plasmas and the argon–hydrogen plasmas, respectively. In the conditions of this study, Six species of Ar, Ar^+, O, O_2, O^+, and e^- in argon–oxygen plasmas, six species of Ar, Ar^+, H, H_2, H^+, and e^- in argon–hydrogen plasmas are considered to be the dominant reactants from estimation of the equilibrium composition using FACT (Center for Research in Computational Thermochemistry).

The dissociation and ionization rates can be calculated by Eq. (1). The constants in Eq. (1) are presented in Tables 1 and 2 taken from Refs. [16–18].

$$k_f = a_l T^{b_l} \exp(-c_l/T). \quad (1)$$

The ionization rate of reaction no. 6 in the tables can be calculated by Eq. (2), which is taken from Ref. [19].

$$k_f = 1.68 \times 10^{-20} T^{1.5} \left(\frac{135300}{T} + 2\right) \exp\left(-\frac{135300}{T}\right). \quad (2)$$

The recombination rate constants were calculated using the equilibrium constants.

Particularly in a low temperature oxygen plasma such as an atmospheric non-equilibrium plasma, the production of ozone can be considerable. However, the existence of ozone does not affect the transport properties of the thermal plasma under the operating conditions in this study. Thus, the elementary chemical reactions shown in Table 1 are reasonable enough.

Table 1
Chemical reactions in argon–oxygen plasmas

No.	Reaction	a_l	b_l	c_l
1	$O_2 + O_2 \rightarrow O + O + O_2$	2.0×10^{21}	−1.5	59,500
2	$O_2 + O \rightarrow O + O + O$	1.0×10^{22}	−1.5	59,500
3	$O_2 + Ar \rightarrow Ar + O + O$	1.0×10^{22}	−1.5	59,500
4	$O_2 + e^- \rightarrow O + O + e^-$	9.68×10^{22}	−2.0	59,500
5	$O + e^- \rightarrow O^+ + e^- + e^-$	3.91×10^{33}	−3.78	158,500
6	$Ar + e^- \rightarrow Ar^+ + e^- + e^-$	k_f was taken from Ref. [19]		

Table 2
Chemical reactions in argon–hydrogen plasmas

No.	Reaction	a_l	b_l	c_l
1	$H_2 + H_2 \rightarrow H + H + H_2$	8.58×10^{12}	0.5	46,600
2	$H_2 + H \rightarrow H + H + H$	2.58×10^{12}	0.5	46,600
3	$H_2 + Ar \rightarrow Ar + H + H$	2.23×10^{12}	0.5	46,600
4	$H_2 + e^- \rightarrow H + H + e^-$	2.23×10^{12}	0.5	46,600
5	$H + e^- \rightarrow H^+ + e^- + e^-$	1.51×10^{31}	−3.0	158,000
6	$Ar + e^- \rightarrow Ar^+ + e^- + e^-$	k_f was taken from Ref. [19]		

The dependent temperature T in the above equations corresponds to T_e if one of the reactants is the electron. In other cases, the dependent temperature T is set to T_h.

2.3. Model and assumptions

The geometry of the calculation domain of the induction plasma torch was shown in Fig. 3 and the operating conditions are summarized in Table 3. The plasma torch consists of a water-cooled quartz tube and a water-cooled induction coil. The coil consists of three turns and applies the induction frequency at 4 MHz to the plasma. The actual power level was assumed to be 5 kW. Argon–oxygen (oxygen 3%) or argon–hydrogen (hydrogen 3%) mixture is injected as the plasma supporting gas (13 NL/min) and as the sheath gas (20 NL/min). The sheath gas injected with swirl from the outer slots protects the inner surface of the quartz tube.

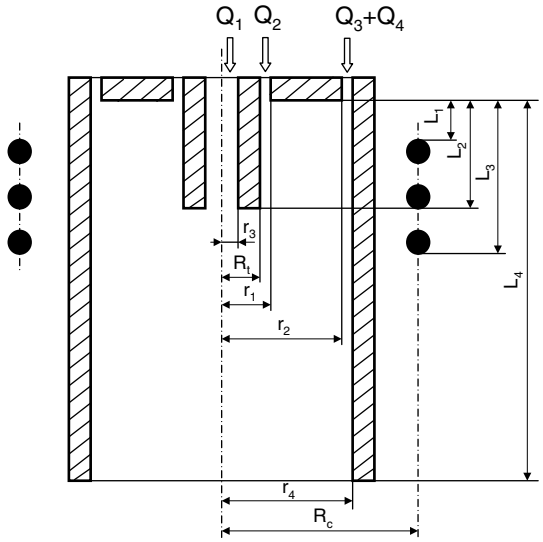

Fig. 3. Geometry of calculation domain of induction plasma torch.

Table 3
Torch characteristic dimensions and operational condition

Torch power	5 kW
Work frequency	4 MHz
Reactor pressure	101.3 kPa
Coil radius	32 mm
Coil turn number	3
Wall thickness of quartz tube	1.5 mm
Distance to frontal end of coil (L_1)	19 mm
Distance to rear end of coil (L_3)	65 mm
Insertion length of probe (L_2)	45 mm
Torch length (L_4)	190 mm
Outer radius of inner slot (r_1)	6.5 mm
Outer radius of outer slot (r_2)	21 mm
Inner radius of injection tube (r_3)	1 mm
Inner radius of quartz tube (r_4)	22.5 mm
Outer radius of injection tube (R_t)	4.5 mm
Flow rate of carrier gas (Q_1)	0 l/min
Flow rate of plasma gas (Q_2)	3 l/min
Flow rate of plasma gas (Q_3)	10 l/min
Flow rate of sheath gas (Q_4)	20 l/min

The calculations are based on the following assumptions to derive the governing equations: (a) steady-state laminar flow; (b) axial symmetry; (c) optically thin; (d) negligible viscous dissipation in energy equation; (e) negligible displacement current in comparison with the conductive current; (f) negligible flow-induced electric field.

These assumptions were adopted only for the simplicity. The effect of turbulence was reported by Chen and Boulos [20]. They reported that most of the flow fields in induction plasmas were laminar at the Reynolds number equal to 625 at the gas inlet, while the turbulence effect was large at the Reynolds number equal to 3125. The flow fields of the present induction plasmas can be considered as laminar since the inlet Reynolds number is 350 in this study.

2.4. Governing equations and boundary conditions

The fields of flow, temperature, and concentration in the induction thermal plasmas were determined by solving the two-dimensional continuity, momentum, energy, and species conservation equations coupled with the Maxwell's equations. Chemical reactions of the dissociation and recombination as well as the ionization were taken into account in this modeling.

Continuity

$$\nabla \cdot (\rho \mathbf{u}) = 0. \tag{3}$$

Momentum

$$\rho \mathbf{u} \cdot \nabla \mathbf{u} = -\nabla p + \nabla \boldsymbol{\tau} + \mathbf{J} \times \mathbf{B}. \tag{4}$$

The last term in the right-hand side expresses the Lorentz force.

Energy (heavy particle)

$$\rho \mathbf{u} \cdot \nabla h = \nabla \cdot (\lambda_{\mathrm{tr}}^{\mathrm{h}} \nabla T_{\mathrm{h}}) + \sum_{i(i \neq \mathrm{e})}^{N} \nabla \cdot (\rho D_i^{\mathrm{m}} h_i \nabla Y_i) - \sum_{l(\beta_{\mathrm{e}l}^{\mathrm{f}} \cdot \beta_{\mathrm{e}l}^{\mathrm{r}} = 0)}^{L} \Delta Q_l + E_{\mathrm{eh}}. \tag{5}$$

The last term is the energy exchange between electrons and heavy particles. The energy exchange term can be estimated from Eq. (6).

$$E_{\mathrm{eh}} = \sum_{i \neq \mathrm{e}} \frac{3}{2} \mathrm{k} (T_{\mathrm{e}} - T_{\mathrm{h}}) \frac{2 m_i m_{\mathrm{e}}}{(m_i + m_{\mathrm{e}})^2} \nu_{\mathrm{e}i}. \tag{6}$$

Energy (electron)

$$\frac{5}{2} \mathrm{k} \nabla (\mathbf{u} n_{\mathrm{e}} T_{\mathrm{e}}) = \nabla \cdot (\lambda_{\mathrm{tr}}^{\mathrm{e}} \nabla T_{\mathrm{e}}) - \frac{5\mathrm{k}}{2 m_{\mathrm{e}}} \nabla (T_{\mathrm{e}} \Gamma_{\mathrm{e}}) - \sum_{l(\beta_{\mathrm{e}l}^{\mathrm{f}} \cdot \beta_{\mathrm{e}l}^{\mathrm{r}} \neq 0)}^{L} \Delta Q_l + \mathbf{J} \cdot \mathbf{E} - q_{\mathrm{r}} - E_{\mathrm{eh}} \tag{7}$$

where $\mathbf{J} \cdot \mathbf{E}$ expresses the Joule heating.

Species

$$\rho \mathbf{u} \cdot \nabla Y_i = \nabla \cdot (\rho D_i^{\mathrm{m}} \nabla Y_i) + R_{\mathrm{r}_i} \quad (8)$$

where D^{m} is the effective diffusion coefficient [21], and R_{r} is the source term owing to the dissociation, recombination and ionization. In these equations, the conduction current **J**, the magnetic flux density **B**, and the electric field intensity **E** were obtained from Maxwell's equations. The electromagnetic (EM) fields in this study were analyzed on the basis of the two-dimensional modeling approach with the electric field intensity as the fundamental EM field variable [22].

The boundary conditions along the centerline were set to ensure axial symmetry. At the wall of the plasma torch, no slip conditions are maintained for the velocity, and the concentrations have zero gradient. The heavy particle temperature at the inside wall of the plasma torch was calculated assuming the outside wall was maintained at 300 K by water cooling. The electron temperature at the inside wall and torch inlet of the plasma is set zero gradient. The injection tube was assumed to be at 500 K. The outflow boundary conditions at the torch were assumed that the gradient of the variables are zero. The sheath gas has the swirl velocity component. Each gas stream has the constant axial velocity with zero radial velocity having temperature at 300 K. The associated boundary conditions for the EM fields are identical to those proposed by Chen and Pfender [22].

2.5. Calculation procedure

The governing conservation equations were solved by using SIMPLER (Semi-Implicit Method for Pressure Linked Equation Revised) algorithm [23]. The governing equations and the electric field intensity equation with the associated boundary conditions were discretized into the finite difference form using the control-volume technique. Non-uniform grid points 30 by 30 were used for radial and axial directions, respectively. Grids are made finer close to the center and the coil region. Thermodynamic and transport properties were calculated from the temperature and the compositions at each position in the calculation domain at each iteration step.

3. Calculation results

Computations were performed for the pure argon, the argon–oxygen (oxygen 3%), and the argon–hydrogen (hydrogen 3%) plasmas operated under atmospheric pressure.

Fig. 4(a) and (b) shows the calculated temperature fields of T_{e} and T_{h} in an argon plasma, respectively. In the coil region, both T_{e} and T_{h} have high-values above 9000 K. T_{e} near the torch wall of coil region has the higher values than T_{h}. The temperature difference can also be found in Fig. 5 for the radial distributions of T_{e} and T_{h} by the different three models at the center of the coil at the axial

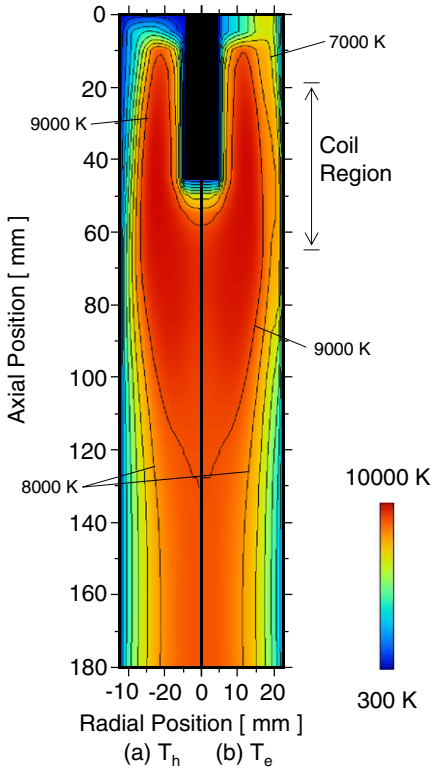

Fig. 4. Comparison of (a) electron temperature and (b) heavy particle temperature by 2T-CNE model in an argon plasma. All isotherms are divided by 1000 K.

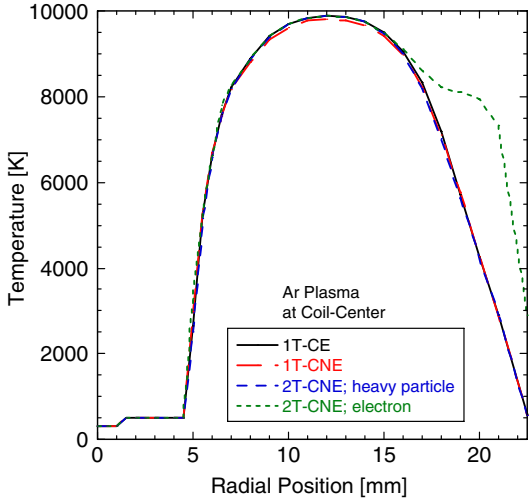

Fig. 5. Radial temperature distributions by three different models in argon plasma at the center of the coil.

position of 40 mm. T_{e} is almost the same with T_{h} at $r < 17$ mm, which means that the thermal equilibrium state is sustained around the torch axis. On the contrary, T_{e} is higher than T_{h} at $r > 17$ mm, indicating that the region near the torch wall is in the thermal-non-equilibrium state. Fig. 6 presents the radial distributions of T_{e} and T_{h} at 180 mm from the torch inlet. Large differences between

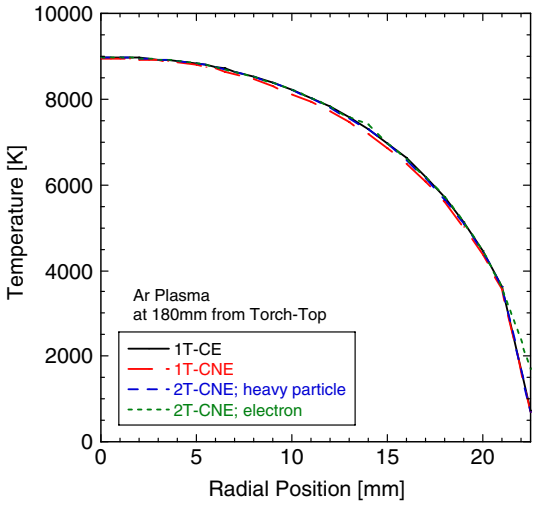

Fig. 6. Radial temperature distributions by three different models in argon plasma at 180 mm from the torch-top.

T_e and T_h vanish at this axial position. Thus, thermal equilibrium is almost established around the downstream region.

Fig. 7(a) and (b) demonstrates the calculated temperature fields of T_e and T_h of the argon–oxygen plasma, respectively. Both T_e and T_h have high-values above 9000 K in the high-temperature region, although T_e near the torch wall of coil region has higher values than T_h. Fig. 8 indicates that T_e is almost the same as T_h at $r < 16$ mm for three models at the center of the coil at the axial position of 40 mm. In contrast, at $r > 16$ mm, the difference between T_e and T_h is larger than that in a pure argon plasma which means that an argon–oxygen plasma is in a comparatively thermal non-equilibrium state. Fig. 9(a) and (b) represents the calculated streamlines and oxygen atom distributions, respectively. The gas flow is bent to the center around the coil region due to the Lorentz force. Oxygen atoms exist broadly in the torch because of the low dissociation energy of oxygen molecules. Fig. 10

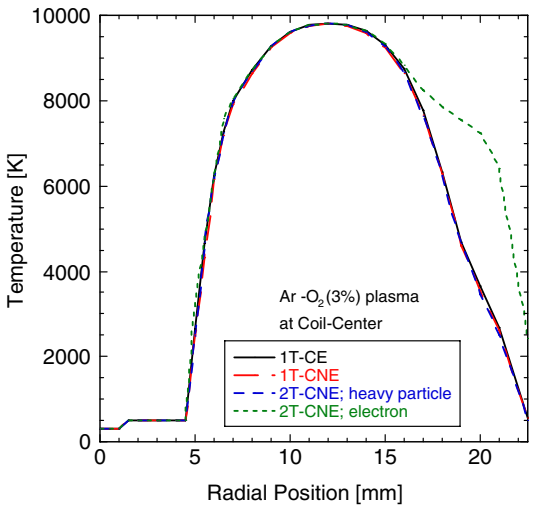

Fig. 8. Radial temperature distributions by three different models in argon–oxygen plasma at the center of the coil.

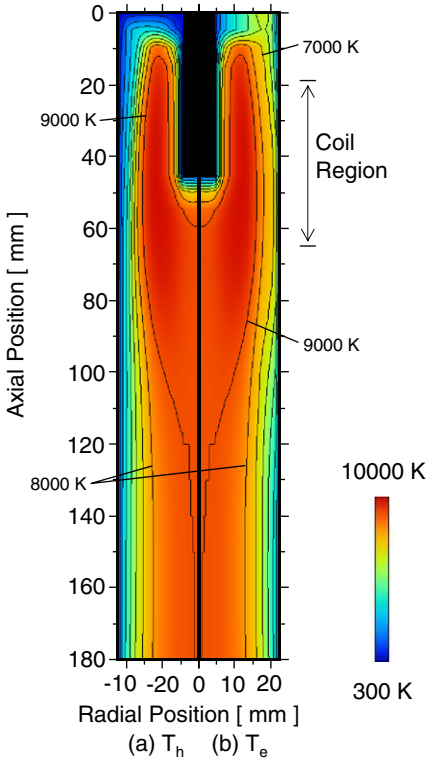

Fig. 7. Comparison of (a) electron temperature and (b) heavy particle temperature by 2T-CNE model in argon–oxygen plasma. All isotherms are divided by 1000 K.

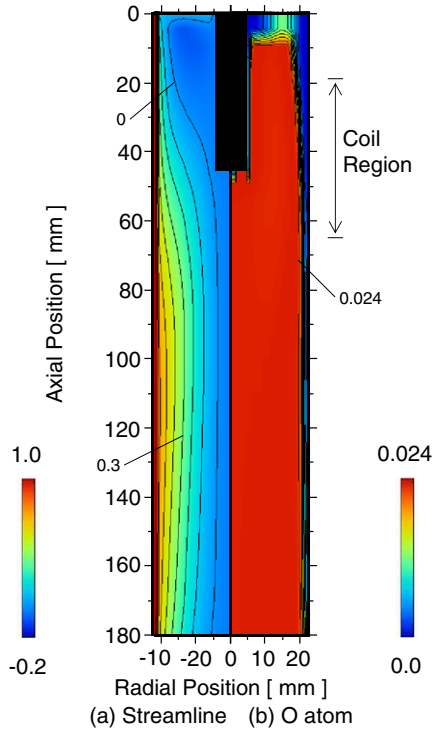

Fig. 9. (a) Streamline and (b) oxygen atom distribution by 2T-CNE model in argon–oxygen plasma. Streamlines are divided by 0.1. Oxygen atom contour is divided by 0.003.

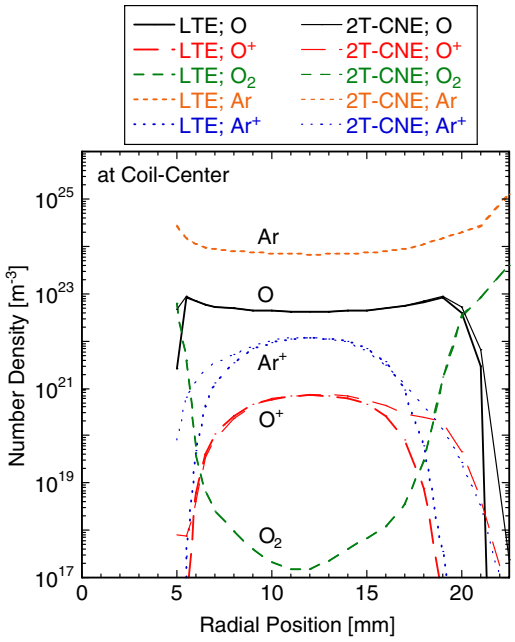

Fig. 10. Comparison of number densities between LTE and 2T-CNE model in argon–oxygen plasma at the center of the coil.

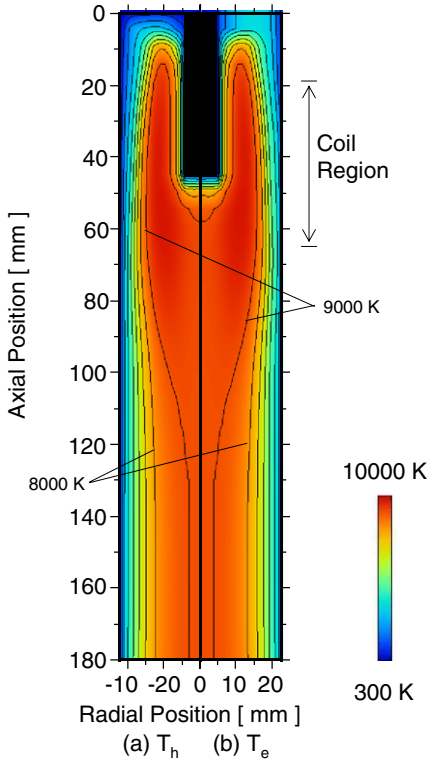

Fig. 11. Comparison of (a) electron temperature and (b) heavy particle temperature by 2T-CNE model in argon–hydrogen plasma. All isotherms are divided by 1000 K.

presents the radial distributions of the number density at the center of the coil by the LTE and 2T-CNE models. Near the torch wall, deviations from the equilibrium composition are obvious especially for oxygen atoms and ions.

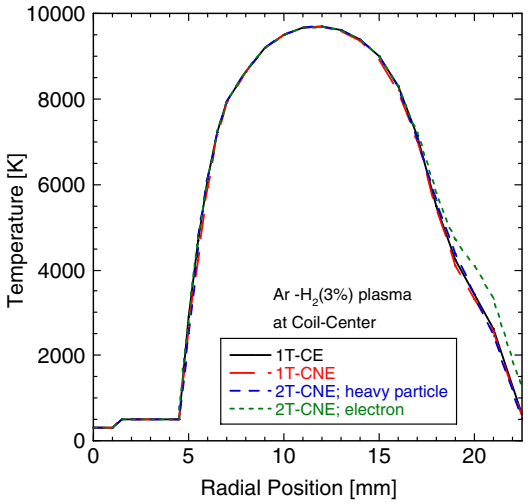

Fig. 12. Radial temperature distributions by three different models in argon–hydrogen plasma at the center of the coil.

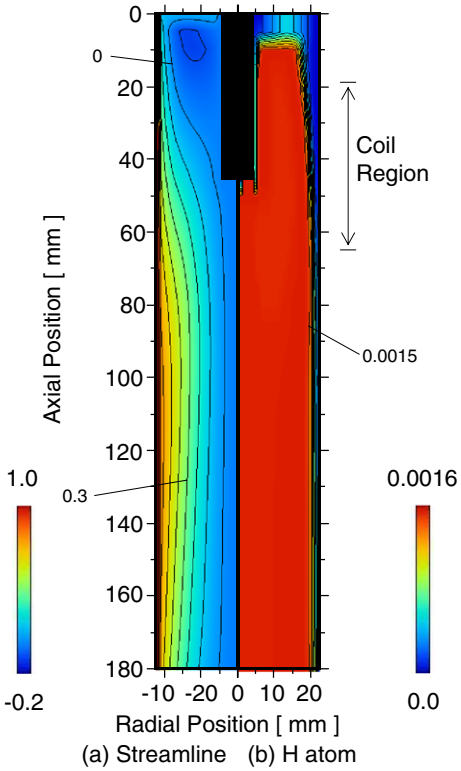

Fig. 13. (a) Streamline and (b) hydrogen atom distribution by 2T-CNE model in argon–hydrogen plasma. Streamlines are divided by 0.1. Hydrogen atom contour is divided by 0.0002.

Fig. 11(a) and (b) exhibits the calculated temperature fields of T_e and T_h of the argon–hydrogen plasma, respectively. In the high-temperature region, both T_e and T_h have higher temperature than 9000 K, similarly in the argon and argon–oxygen plasmas. However, deviation of T_e from T_h is smaller than the cases of the argon and the argon–oxygen plasmas. Fig. 12 indicates the radial distributions of T_e and T_h by the three models at the center of the coil at the axial

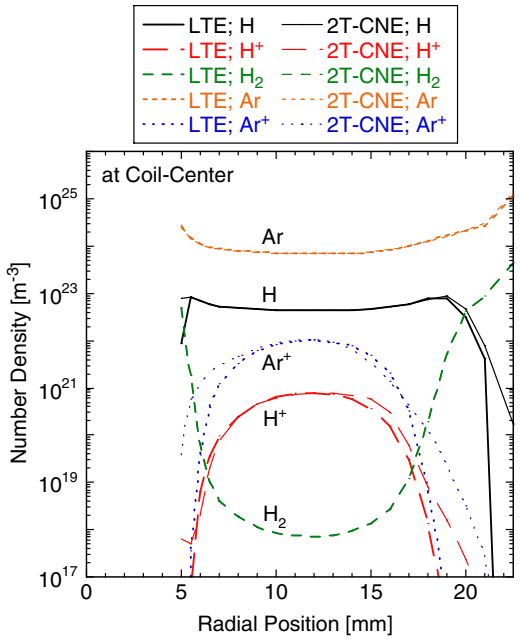

Fig. 14. Comparison of number densities between LTE and 2T-CNE model in argon–hydrogen plasma at the center of the coil.

position of 40 mm. Thermal equilibrium is obtained at $r < 18$ mm. At $r > 18$ mm, the difference between T_e and T_h is smaller than that in a pure argon and an argon–oxygen plasmas. For instance, T_e at $r = 20$ mm is higher by 1000 K compared with T_h. The calculated streamlines of the argon–hydrogen plasma in Fig. 13(a) shows the streamlines is almost the same as the argon–oxygen plasma. In Fig. 13(b), hydrogen atoms exist broadly in the torch because of the low dissociation energy of hydrogen molecules. Fig. 14 presents the radial distributions of the number density at the center of the coil by the LTE and the 2T-CNE models. Along with the argon–oxygen plasma, deviations from the equilibrium composition, especially hydrogen atoms and ions, exist near the torch wall.

4. Discussion

4.1. Deviation from equilibrium

The numerical analysis revealed that thermal non-equilibrium existed near the torch wall of the coil region in an argon and an argon–oxygen plasmas, while the thermal non-equilibrium was weak in an argon–hydrogen plasma. To investigate the thermal non-equilibrium, the energy balance of electrons in an argon–oxygen plasma at the center of the coil was calculated as shown in Fig. 15: the energy exchange between electron and heavy particles, the radiation heat loss, the Joule heating rate, and the reaction energy. The energy exchange between the electrons and the heavy particles is balanced to the Joule heating rate at $r > 16$ mm in the region of $T_e \neq T_h$.

$$\sum_{i \neq e} \frac{3}{2} k (T_e - T_h) \frac{2 m_i m_e}{(m_i + m_e)^2} \nu_{ei} = \mathbf{J} \cdot \mathbf{E} \tag{9}$$

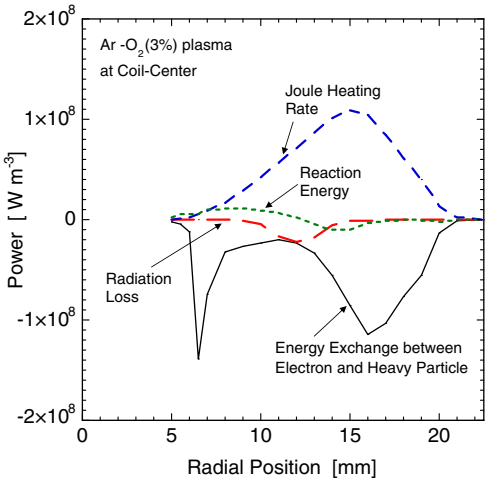

Fig. 15. Energy balance of electrons in an argon–oxygen plasma at the center of the coil.

where $2 m_i m_e / (m_i + m_e)^2 \nu_{ei}$ is the energy exchange ratio, ν_{ei} is the collision frequency between electrons and heavy particles, written in

$$\nu_{ei} = n_i n_e \overline{\Omega}_{ei}^{(1,1)} \left[\frac{8 k T_e (m_e + m_i)}{\pi m_e m_i} \right] \tag{10}$$

where $\overline{\Omega}_{ei}^{(1,1)}$ is the collision integrals between an electron and heavy particles. Since the injection tube and the torch wall are water-cooled, the temperature boundary layers with the steep gradient are generated. In these regions, the electrons that obtain energy by Joule heating diffuse toward the lower temperature side and exchange the energy with the heavy particles by collision.

Large $(T_e - T_h)$ results from the small energy exchange ratio: $2 m_i m_e / (m_i + m_e)^2 \nu_{ei}$ from Eq. (9). The energy exchange ratio depends on the collision frequency and the mass of atoms. Fig. 16 shows the total collision frequency between electrons and heavy particles at the center of the

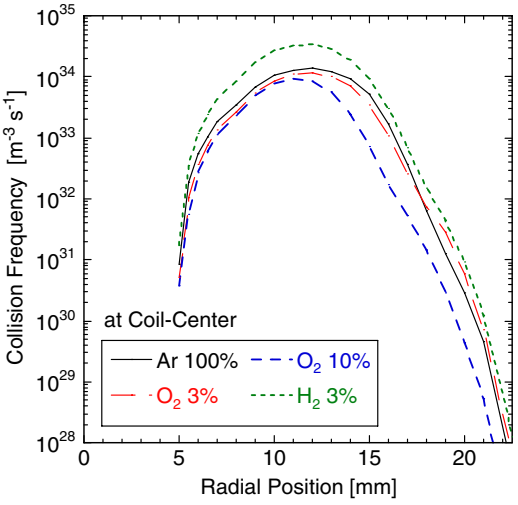

Fig. 16. Collision frequency between electrons and heavy particles at the center of the coil.

coil. That of an argon–hydrogen plasma is large due to the large collision integral between an electron and a hydrogen atom [24]. The large total collision frequency and the small mass of hydrogen near the torch wall lead to the high-energy transfer between electrons and heavy particles, which result in small deviation from T_e and T_h. On the other hand, the small collision frequency between electrons and heavy particles near the torch wall promotes a strong thermal non-equilibrium state such as a pure argon and an argon–oxygen plasmas.

4.2. Evaluation of non-equilibrium state

The deviation from the equilibrium which depends on the plasma conditions was presented in thermal plasmas. Therefore, two parameters are proposed to evaluate the non-equilibrium state in thermal plasmas.

The degree of CNE (chemical non-equilibrium) was introduced to evaluate chemical non-equilibrium in plasmas.

Dissociation

$$\delta^{\mathrm{D}}_{\mathrm{O}} = \frac{[\mathrm{O}]^2}{[\mathrm{O}_2]K_{\mathrm{O}}}, \quad \delta^{\mathrm{D}}_{\mathrm{H}} = \frac{[\mathrm{H}]^2}{[\mathrm{H}_2]K_{\mathrm{H}}}. \tag{11}$$

Ionization

$$\delta^{\mathrm{I}}_{\mathrm{O}^+} = \frac{[\mathrm{O}^+][\mathrm{e}^-]}{[\mathrm{O}]K_{\mathrm{O}^+}}, \quad \delta^{\mathrm{I}}_{\mathrm{H}^+} = \frac{[\mathrm{H}^+][\mathrm{e}^-]}{[\mathrm{H}]K^+_{\mathrm{H}}}, \tag{12}$$

$$\delta^{\mathrm{I}}_{\mathrm{Ar}^+} = \frac{[\mathrm{Ar}^+][\mathrm{e}^-]}{[\mathrm{Ar}]K_{\mathrm{Ar}^+}} \tag{13}$$

where $[M]$ is the molar concentration of species M in the plasma. Value of $\delta = 1$ represents the complete equilibrium state. Values of $\delta > 1$ and $\delta < 1$ express overpopulation of products and underpopulation of reactants, respectively.

Furthermore, Damkohler number which indicates the relation between the diffusion rate and the chemical reaction rate was introduced as follows:

$$\varsigma = \frac{\tau_{\mathrm{d}}}{\tau_{\mathrm{r}}}. \tag{14}$$

τ_{d} is the characteristic time of diffusion defined as

$$\tau_{\mathrm{d}} = \frac{(r_{\mathrm{w}} - r)^2}{D^{\mathrm{m}}_i} \tag{15}$$

where $(r_{\mathrm{w}} - r)$ is the distance to the torch wall.

τ_{r} is the characteristic time of reaction defined as

$$\tau_{\mathrm{r}} = \frac{1}{k_{\mathrm{f}}[M]}. \tag{16}$$

In these definition, $\delta = 1$, $\varsigma \to \infty$ express equilibrium, $\delta \neq 1$, $\varsigma \to 0$ indicate non-equilibrium. Both the degree of CNE and the Damkohler express the equilibrium state in the plasma. The degree of CNE is an indication to present the degree of chemical equilibrium state directly. But the estimation of degree of CNE requires number density distributions estimated by the numerical modeling of plasmas. In contrast, the Damkohler number can be estimated easily without the complicated modeling, because the Damkohler number can be calculated only from the average properties of the plasma.

Damkohler number and the degree of CNE due to dissociation at the center of the coil region are shown in Fig. 17. The result of an argon–nitrogen plasma was taken from Ref. [11]. Near the torch wall, the degree of dissociation is high, subsequently the corresponding Damkohler number is small. Accordingly, Damkohler number is strongly related to the degree of CNE. In an argon–nitrogen plasma, chemical non-equilibrium is more noticeable near the torch wall than that in an argon–oxygen and an argon–hydrogen plasma due to high dissociation energy of N_2. The corresponding Damkohler number is smaller in an argon–nitrogen plasma. Therefore, Damkohler number can be used as the indication to evaluate the degree of chemical non-equilibrium.

Fig. 18 shows the degree of CNE and Damkohler number due to ionization at the center of the coil region including the result of an argon–nitrogen plasma [11].

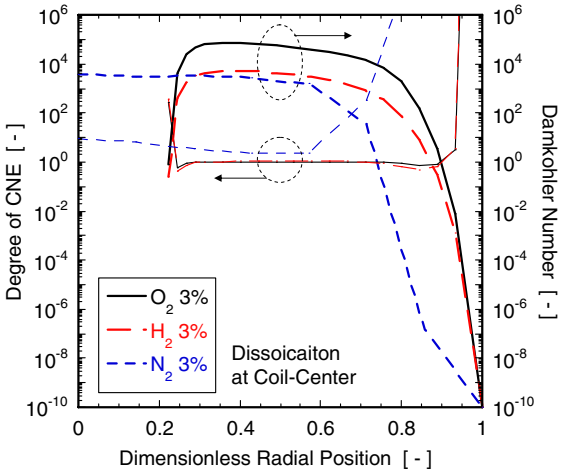

Fig. 17. Radial distribution of degree of CNE and Damkohler number due to dissociation at the center of the coil.

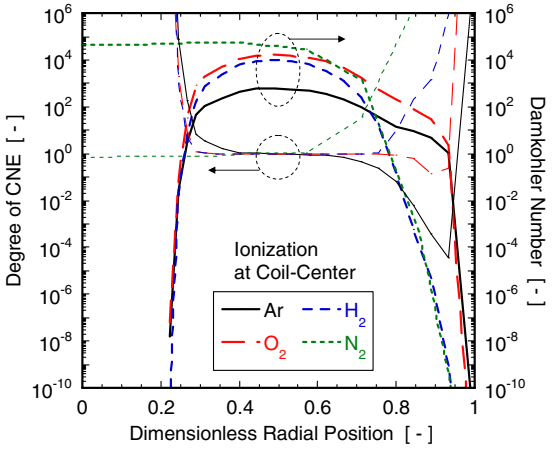

Fig. 18. Radial distribution of degree of CNE and Damkohler number due to ionization at the center of the coil.

The degrees of CNE in all plasmas deviate from unity indicating an ionization equilibrium state where the degrees of ionization are very small at the dimensionless radial diameter larger than 0.8. Near the torch wall, Domkohler numbers show large due to the large ionization rate in a pure argon and an argon–oxygen plasmas which have the large temperature difference between electrons and heavy particles. An argon–hydrogen and an argon–nitrogen plasmas show smaller Damkohler numbers near the torch wall due to the small temperature difference between electrons and heavy particles.

5. Conclusions

Two-temperature and chemically-non-equilibrium modeling for an argon–oxygen and an argon–hydrogen induction thermal plasmas considering the effects of diffusion and finite reaction rates without local thermodynamic equilibrium (LTE) assumption demonstrates the following results.

Considerable thermal non-equilibrium exists near the torch wall of the coil region in an argon and an argon–oxygen plasmas, while the degree of thermal non-equilibrium is weak in an argon–hydrogen plasma. This is mainly due to the larger collision frequency between electrons and hydrogen heavy particles, and the small mass of hydrogen resulting in the high energy exchange ratio. As a result, the present modeling reveals that thermal non-equilibrium and chemical non-equilibrium exist near the torch wall.

Furthermore, Damkohler number and the degree of CNE were proposed to present the non-equilibrium state in thermal plasmas. Especially, Damkohler is useful indication to evaluate the degree of chemical non-equilibrium in plasmas, because the Damkohler number can be estimated easily without the complicated modeling.

Acknowledgement

This research was supported by the Ministry of Education, Science, Sports and Culture, Grant-in-Aid for Scientific Research (B).

References

[1] S.L. Girshick, W. Yu, Radio-frequency induction plasmas at atmospheric pressure: Mixtures of hydrogen, nitrogen, and oxygen with argon, Plasma Chem. Plasma Process. 10 (1990) 515–529.
[2] S.L. Girshick, C. Li, W. Yu, H. Han, Fluid boundary layer effects in atmospheric–pressure plasma diamond film deposition, Plasma Chem. Plasma Process. 13 (1993) 169–187.
[3] T. Watanabe, N. Tonoike, T. Honda, A. Kanzawa, Flow, temperature and concentration fields in reactive plasmas in an inductively coupled RF discharge. Characteristics in argon–oxygen and argon–nitrogen thermal plasmas, J. Chem. Eng. Japan 24 (1991) 25–32.
[4] T. Watanabe, A. Kanzawa, T. Ishigaki, Y. Moriyoshi, Thermal plasma treatment of titanium carbide powders: Part I. Numerical analysis of powder behavior in argon–hydrogen and argon–nitrogen radio frequency plasmas, J. Mater. Res. 11 (1996) 2598–2610.
[5] M. Desilets, B. Davies, G. Soucy, P. Proulx, Mixing study in an inductive plasma reactor: comparison between model calculations and experimental results, Can. J. Chem. Eng. 76 (1998) 707–716.
[6] M. Sakano, T. Watanabe, M. Tanaka, Numerical and experimental comparison of induction thermal plasma characteristics between 0.5 MHz and 4 MHz, J. Chem. Eng. Japan 32 (1999) 619–625.
[7] Y. Tanaka, T. Sakuta, Chemically non-equilibrium modeling of N_2 thermal ICP at atmospheric pressure using reaction kinetics, J. Phys. D 35 (2002) 468–476.
[8] T. Watanabe, N. Sugimoto, Numerical analysis of oxygen induction thermal plasmas with chemically non-equilibrium assumption for dissociation and ionization, Thin Solid Films 457 (2004) 201–208.
[9] N. Atsuchi, M. Shigeta, T. Watanabe, Modeling of non-equilibrium argon–oxygen Induction plasmas under atmospheric pressure, Int. J. Heat Mass Transfer 49 (2006) 1073–1082.
[10] J. Mostaghimi, M.I. Boulos, Effect of frequency on local thermodynamic equilibrium conditions in an inductively coupled argon plasma at atmospheric pressure, J. Appl. Phys. 68 (1990) 2643–2648.
[11] Y. Tanaka, Two-temperature chemically non-equilibrium modeling of high-power Ar–N_2 inductively coupled plasmas at atmospheric pressure, J. Phys. D 37 (2004) 1190–1205.
[12] J.O. Hirschfelder, C.F. Curtiss, R.B. Bird, Molecular Theory of Gases and Liquids, John Willy, New York, 1964.
[13] J.N. Bulter, R.S. Brokaw, Thermal conductivity of gas mixtures in chemical equilibrium, J. Chem. Phys. 26 (1957) 1636–1643.
[14] C. Muckenfuss, C.F. Curtiss, Thermal conductivity of multicomponent gas mixtures, J. Chem. Phys. 29 (1958) 1273–1277.
[15] R.S. Devote, Simplified expressions for the transport properties of ionized monatomic gases, Phys. Fluids 10 (1967) 2105–2112.
[16] C. Park, A review of reaction rates in high-temperature air, AIAA Paper (1989) 89–1740.
[17] C. Park, Assessment of two-temperature kinetic model for ionizing air, J. Thermophys. Heat Transfer 3 (1989) 233–244.
[18] J.H. Park, E. Pfender, C.H. Chang, Reduction of chemical reactions in nitrogen and nitrogen–hydrogen plasma jets flowing into atmospheric air, Plasma Chem. Plasma Process. 20 (2000) 165–181.
[19] M. Hoffert, H. Lien, Quasi-one-dimensional nonequilibrium gas dynamics of partially ionized two-temperature argon, Phys. Fluids 10 (1967) 1769–1777.
[20] K. Chen, M.I. Boulos, Turbulence in induction plasma modeling, J. Phys. D 27 (1994) 946–952.
[21] R.B. Bird, W.E. Stewart, E.N. Lightfoot, Transport Phenomena, John Wiley & Sons, New York, 1960.
[22] X. Chen, E. Pfender, Modeling of RF plasma torch with a metallic tube inserted for reactant injection, Plasma Chem. Plasma Process. 11 (1991) 103–128.
[23] S.V. Patanker, Numerical Heat transfer and Fluid Flow, McGraw-Hill, New York, 1980.
[24] J.R. Stallcop, E. Levin, H. Partridge, Transport properties of hydrogen, J. Thermophys. Heat Transfer 12 (1998) 514–519.